SCIENTIA

Peer Reviewed National Science Journal

Published by

MERCY COLLEGE

PALAKKAD 678006, KERALA, INDIA

Bismuth triiodide: Ab-initio simulations to spray cast thin films for optoelectronic applications

Sebin Devasia[1], Anjali A. Ramachandran[1], S. Shaji[1,2], D. A. Avellaneda[1], J.A. Aguilar Martinez[1,3], Bindu Krishnan[1,2,*]

[1]Facultad de Ingeniería Mecánica y Eléctrica, Universidad Autónoma de Nuevo León. San Nicolás de los Garza, Nuevo León, México, 66455.

[2]Centro de Innovación, Investigación y Desarrollo en Ingeniería y Tecnología (CIIDIT)- Universidad Autónoma de Nuevo León, Parque de Investigación e Innovación Tecnológica (PIIT), Apodaca, Nuevo León, 66600, México.

[3]Centro de Investigación e Innovación en Ingeniería Aeronáutica (CIIA); Facultad de Ingeniería Mecánica y Eléctrica, Carretera a Salinas Victoria, Apodaca, Nuevo León, 66600, México.

Abstract

In this report, we discuss the computational as well as experimental research done on the metal halide perovskite bismuth iodide.We employed DFT calculations to explain the spin-orbit coupling effects in BiI_3 in lowering the CBM and thus, obtained an optical band gap of 1.44 eV having indirect nature. Further, we synthesized BiI_3 powder from bismuth nitrate and potassium iodide. Then, we fabricated BiI_3 thin films via a scalable ultrasonic spray deposition method using the powder as precursor. Further, we studied the structure, morphology, composition, absorption and photoresponse of the thin film. The film possessed dendritic-like morphology with an indirect bandgap of 1.42 eV. Moreover, it displays a very good response to the illumination from white light and LEDs with a sensitivity of 4890 %.

Keywords: Bismuth iodide, DFT, Thin films, Ultrasonic spray coating, photoresponse.

Introduction

The layered bismuth tri-iodide (BiI_3) with its intermediate bandgap from strong spin-orbit coupling is an interesting semiconductor for structural and electronic exploration[1–8]. Their potential semiconducting character is complemented by a rich structural diversity in the inorganic framework arising from the different degrees of distortion of bismuth halide octahedra (BiX_6). Such bismuth halide octahedra can connect by corner-, edge-, face- sharing to form distinct networks of bismuth halogen anions like BiX_4^-, BiX_5^{2-}, BiX_6^{3-}, $Bi_2X_9^{3-}$, $Bi_2X_{11}^{5-}$, $Bi_{13}X_{12}^{3-}$, $Bi_4X_{18}^{6-}$, $Bi_5X_{18}^{3-}$, $Bi_6X_{22}^{4-}$ and $Bi_8X_{30}^{6-1}$. Taking advantage of the intermediate bandgap, high density and high effective atomic number, it has been used for room temperature gamma-ray detection[2], scintillation[3] and x-ray digital imaging[4]. In addition, the material has also found potential applications in photodetectors, LEDs and photovoltaics[5], owing to the recent interests to replace toxic Pb in the hybrid lead halide perovskites.

At room temperature, BiI_3 has a rhombohedral structure which belongs to the trigonal crystal system with six formula units per unit cell. Within each unit cell, BiI_3 adopts a layered structure with highly ionic Bi-I bonds in the layer and weak van der Waals bonding between the layers[8]. As a matter of fact, the non-toxic and stable bismuth (Bi^{3+}) cation has an electronic configuration of $[Xe]4f^{14}5d^{10}6s^26p^0$ which is isoelectronic to Pb^{2+6}. In BiI_3, the vacant Bi 6p orbitals account for the conduction band minimum (CBM) and the occupied Bi 6s and I 5p orbitals for the valence band maximum (VBM). The strong antibonding character of Bi s and I p in the VBM of the material can lead to shallow defect states and longer carrier lifetimes. Besides, strong absorption can be expected

---

* *Corresponding author, E-mail: k_binduk@yahoo.com*

owing to the high density of states of p-orbitals in the conduction band minimum (CBM)[7,9].

Noticeably, the band gap values determined from experimental and computational studies of BiI_3 spread across a wide range of values from 1.43 eV to 2.2 eV. Schluter et al. used the empirical pseudopotential method to calculate the electronic structure of BiI_3 and obtained a direct bandgap of 2.2 eV[10]. However, Yorikawa and Muramatsu observed a much lower bandgap of 1.6652 eV but indirect in nature[11]. The first-principles of linearized augmented plane-wave (LAPW) calculations using three different potentials yielded band gaps of 1.43, 1.67 and 1.82 eV[3]. The band gaps determined by Podreza et al. from the optical and computational methods were indirect with a value of 1.55 and 1.67+/- 0.09 eV, respectively, whereas the spectroscopic ellipsometry results showed a direct transition of 1.94-1.96 eV[8]. Recently, the studies conducted by Ma et al. suggests strong spin-orbit coupling (SOC) in the BiI_3 monolayer leading to an indirect bandgap of 1.57 eV[12].

Predominantly, the earlier studies were focused on the single crystals of BiI_3 synthesized by vapor transport[13,14], Bridgman method[8] and single diffusion techniques [15]. Meanwhile, thin films of BiI_3 have been realized through methods like hot wall technique [16–18], chemical methods [19], thermal evaporation [20,21], physical vapor transport [5,22,25] and mostly by spin coating [20,23,24]. However, such deposition methods cannot promise low-cost devices due to the constraints faced in large scale production. A truly scalable ultrasonic spray coating is indeed a versatile technique that can offer large area deposition at a fast rate and low cost. Ultrasonic spray coater uses a piezoelectric transducer to break the precursor solution into a fine mist of uniform micron sized droplets in contrast to the aperture based conventional spray coaters that utilize compressed air. Consequently, thin films are deposited with better uniformity[25–27]. Lately, the organic lead halide perovskites have been deposited by the method and effectively integrated into photovoltaic structures[28–35] to attain PCE as high as 19.4%[25].

The experimental and computational studies conducted over the time reveal that there is a strong disagreement in the values and nature of the bandgap for the BiI_3. Here, we follow a synergetic approach towards the computational and experimental study of BiI_3 which yielded results that are quite in agreement with each other. We used VASP codes for computation and ultrasonic spray deposition (USD) for fabricating pure BiI_3 thin films. The solution-based synthesis route of thin films relies on nontoxic ethanol solvent different from the widely used dimethylformamide (DMF). Unlike BiI_3 thin films deposited by other methods, the stability and purity of our BiI_3 thin films in ambient conditions as well as their high absorption coefficients are noteworthy.

Materials and Methods

Computational Methods

Initially, a generalized gradient approximation (GGA) to the exchange-correlation energy is used with the Perdew-Burke-Ernzerhof (PBE)[36] functional for geometry optimizations. We used the most reliable VASP electronic structure method[37,38] in the platform of MedeA software[39]. Here, we allowed the relaxation of atomic positions, cell shape and volume to create a stress-free unit cell of BiI_3. The structure was optimized using a plane-wave cutoff energy of 500 eV to relax all the structural parameters until the force and energy were converged to 0.02 eV/Å and 1×10^{-5} eV, respectively. The blocked Davidson algorithm was used for the convergence of electronic iterations. The k-points were sampled at 3×3×3 mesh both for SCF and non-local exchange with the Monkhorst-Pack method. The linear tetrahedron method with Blöchl corrections was used for Brillouin zone integration and the smearing width was 0.2.

Subsequently, we used the minimized structure for the calculation of electronic band structure and density of states (DOS) to determine the optical band gap of BiI_3. The generalized gradient approximation (GGA) in the Perdew-Burke-Ernzerhof (PBEsol) form within the projector augmented wave method[40] was employed as

exchange-correlation functional in the DFT calculation. Further, we included spin-orbit coupling to analyze the effects of heavy Bi and I atoms on the observed optoelectronic properties.

Synthesis of bismuth iodide powder

The BiI_3 powder was prepared by mixing 1M bismuth nitrate ($Bi(NO_3)_3$, 394.99 g/mol) (24.25 g) and 3M potassium iodide (KI, 166.0028 g/mol) (24.9 g) in 50 ml water for the following reaction,
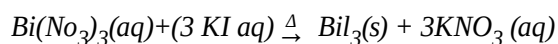
$$Bi(No_3)_3(aq) + (3\ KI\ aq) \xrightarrow{\Delta} BiI_3(s) + 3KNO_3\ (aq)$$

Fig. 1. Bismuth iodide powder obtained from the reaction of
Bi $(NO_3)_3$ with KI.

The BiI_3 precipitate was filtered and washed with distilled water and then dried in a hot air oven at 120°C for 1 h. The brownish-black BiI_3 powder (fig. 1) was carefully grinded and stored.

Deposition of bismuth iodide film by ultrasonic spray method

A 0.01 M precursor solution was prepared by dissolving 0.295 g of BiI_3 powder in 50 ml ethanol after stirring well for 2 h. The deposition was done using the ultrasonic spray pyrolysis coater (CY-USP130-A, Zhengzhou CY Scientific Instrument Co., Ltd.) which employs a 40 kHz, 130 W ultrasonic nozzle for atomization[41]. The cleaned glass substrates were pre-heated to 150°C. The spray rate, air pressure and the current supply for ultrasonic nozzle were set to 6 ml/min., 0.1 MPa and 0.05 A, respectively. The solution was sprayed onto the glass substrates for 30 mins during which the speed of the spray head was 50 mm/s in the x-axis and 20 mm/s in the y-axis. Immediately after deposition, the glass substrates coated with films were transferred from the heater and stored (Fig. 2).

Fig. 2. The as-deposited BiI_3 thin film on glass substrates by ultrasonic spray deposition.

Characterization

The X-ray diffraction study was done with the PANalytical EMPYREAN diffractometer employing Cu Kα radiation (λ=1.5406 Å). The Thermo Scientific K-alpha equipment (Al K_α =) was used for X-ray photoelectron spectroscopy. For the XPS data, a charge correction to the binding energy was done referencing to the C-C/C-H peak of adventitious carbon at 284.6 eV in addition to the charge compensation by a flood gun. Further, the peak modelling was done using the Shirly-type background and the Gaussian-Lorentzian sum function. The film morphology was examined from the scanning electron micrographs obtained using SEM-Hitachi SU8020 equipment. A Jasco V770 spectrophotometer was used for absorption measurements. Photoresponse of the thin film was measured by an arrangement involving a Keithley 6487 Picoammeter, contact electrodes and 50 W tungsten halogen lamp or LEDs.

Results and Discussion
Computational results

The geometry optimized structure of BiI_3 unit cell containing 6 formula units is shown in fig. 3. The bulk BiI_3 structure consists of layers of highly ionic Bi-I bonds stacked in ABC order with weak van der Waals interaction between the layers. The BiI_3 has an R-3H symmetry with 6 Bi atoms at the 6c Wyckoff positions and 18 I atoms occupy the 18f Wyckoff positions.

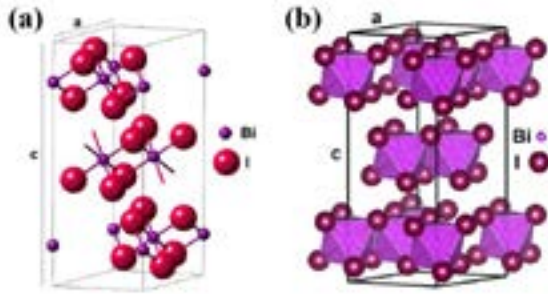The structure optimizations relaxed an energy of -0.019026 eV for $(BiI_3)_2$. The final energy and

Fig. 3. (a) The R-centered hexagonal unit cell of BiI_3 after structural optimization. (b) hexagonal unit cell displaying the high symmetry (BiI_6) octahedra

the density of the unit cell $(BiI_3)_6$ are -68.011136 eV and 5.819 gcm^{-3}, respectively. Further, more parameters related to the optimized cell can be referenced in Table 1.

Table 1. The unit cell parameters obtained from the structure optimization of the BiI_3 unit cell.

Parameter	Original (Å)	Final (Å)	Change (%)
a	7.516	7.523913	0.1
b	7.516	7.523913	0.1
c	20.718	20.595052	-0.6
α	90	90	0
β	90	90	0
γ	120	120	0
Volume	1013.565929	1009.673714	-0.4

Figure 4(i) & (ii) illustrates the electronic band structure for high symmetry directions in the Brillouin zone for the BiI_3 exhibiting the spin-orbit coupling (SOC) effects. It is observed from the calculations that the spin-orbit coupling significantly lowers the conduction band minimum to lower energy, a characteristic of heavy atoms like Bi and I. The calculations without SOC have resulted in a large indirect bandgap of 2.387 eV with valence band maximum near (0.20, 0.20, 0.20) at -0.053 eV and conduction band minimum near (0.40, 0.40, 0.40) at 2.334 eV with respect to the Fermi level. On the other hand, the inclusion of SOC for optical band gap calculation revealed a shorter indirect transition of 1.439 eV between the VBM (0.33,0.33,0.33) and CBM (0,0,0) near the Γ point, in the ZΓ direction.

In addition to the observed indirect transition, low band dispersion in VB suggests the possibility of direct transitions of marginally higher energy. The pronounced band dispersion in CB and the flat VBM indicates a low effective mass of electrons with respect to the holes in BiI_3[42–44]. The calculations suggest that the electrons could be contributing more to the transport properties of the material[45].

Correspondingly, the partial and total density of states from the single point calculations are displayed in fig. 4(a), (b) and (c). A careful analysis
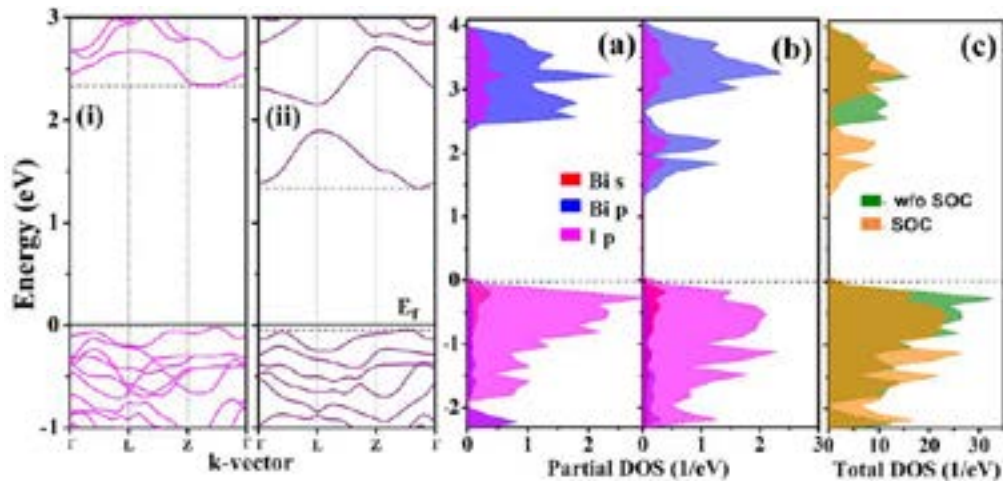

Fig. 4. The band structure for high symmetry directions in the Brillouin zone of BiI_3 (i) without spin-orbit coupling and (ii) with spin-orbit coupling. Corresponding partial density of states for calculations (a) without SOC and (b) with SOC as well as their (c) total density of states.

indicates that the valence band maximum (VBM) is mainly composed of I p states (hybridized with Bi s state) and conduction band minimum (CBM) is composed of Bi p states (hybridized with I p states). Therefore, light-induced excitation from the valence band to the conduction band occurs mainly from the occupied I p with a small Bi s contribution into the empty Bi p +I p states[46]. The high density of states of p orbitals in the conduction band minimum can contribute to strong absorption[7]. Significantly, two additional broad peaks have been emerged in the CB due to the spin-orbit splitting, first one at ~2.18 eV above E_F with a width of ~0.70 eV and the latter at ~1.83 eV with ~0.60 eV width, predominantly composed of Bi p states in hybridization with I p. It is evident from our DFT calculations that the low band-gap observed in BiI_3 is a consequence of strong spin-orbit coupling from the heavy elements, Bi and I.

Bismuth iodide powder

Structural analysis (XRD)

The XRD pattern of the laboratory prepared BiI_3 powder is shown in fig. 5. While most of the diffraction peaks are well in match with the JCPDS file no: 48-1795 of BiI_3, two low intense peaks at 29.64° and 31.64° corresponds to the (102) and (110) planes of tetragonal BiOI phase
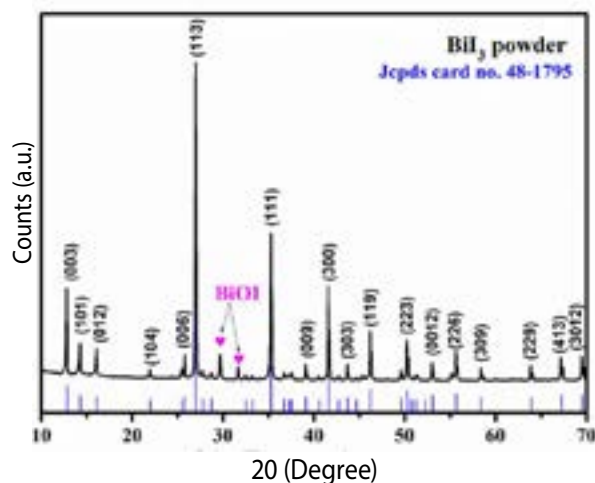

Fig. 5. The XRD pattern of laboratory synthesized BiI_3 powder. The heart shape denotes the peaks from the BiOI phase present in the powder.

(10-0445). Here, the polycrystalline BiI_3 has the rhombohedral structure with the space group R-3, which is usually represented by an R-centered hexagonal unit cell (Fig. 3).The most intense peak was observed at 26.97° corresponding to the (113) plane signifying the preferential orientation of crystallite growth in synthesized powder. Other major peaks observed are from (003), (111) and (300) planes at 12.79°, 35.25° and 41.57°, respectively.

Chemical state analysis (XPS)

The powder samples were dissolved in acetone and then drop-cast on a glass slide for X-ray photoelectron spectroscopy (XPS) measurements. The surface survey spectrum in fig. 6 identifies the presence of Bi, I, O and C and confirms the absence of K, nitrates or any other elemental impurities from the reactants.
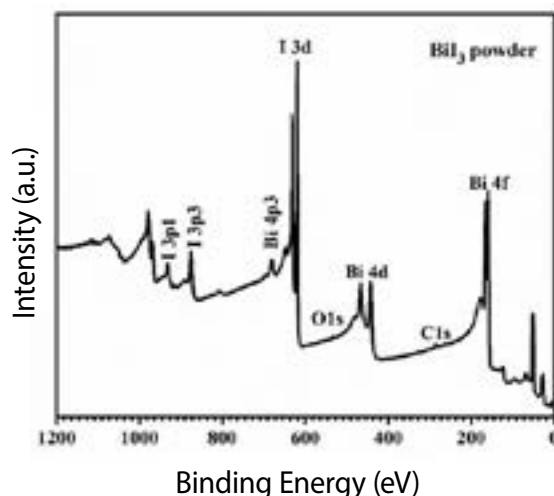

Fig. 6. Survey spectrum collected from the surface of BiI_3 powder drop-cast on a glass substrate.

The high-resolution spectra of Bi and I are illustrated in fig. 7. Bismuth has two peaks at 159.06 and 164.37 eV corresponding to $4f_{7/2}$ and $4f_{5/2}$ levels with a spin-orbit splitting of 5.31 eV which are in agreement with the doublets for Bi^{3+} state in BiI_3[47]. The I $3d_{5/2}$ and I $3d_{3/2}$ are located at 619.36 eV and 630.85 eV with energy splitting of 11.49 eV due to spin-orbit interactions[47]. The 1s state of oxygen has peaks located at 530.28, 531.86 and 533.03 eV. The peak at 533.03 eV
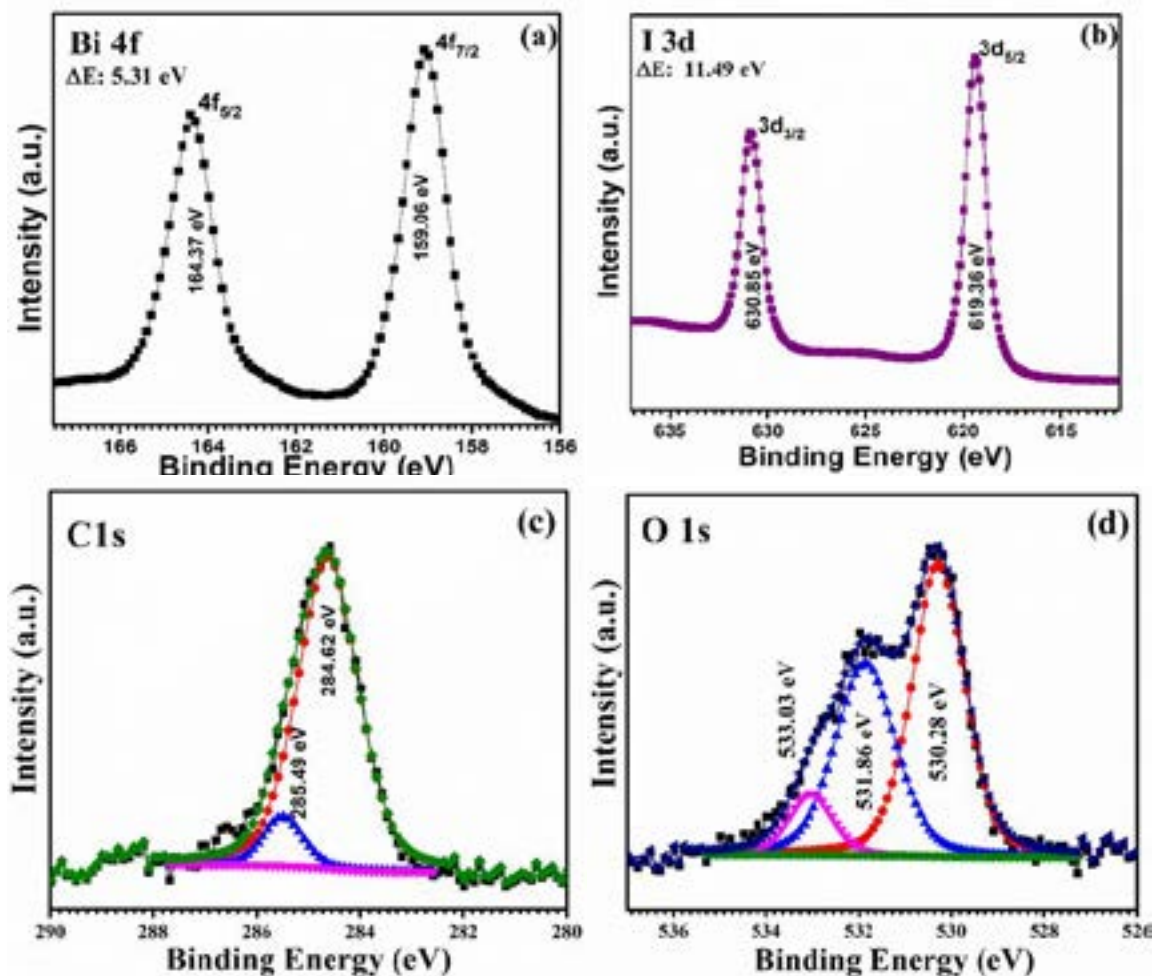
Fig. 7. The high-resolution spectra of (a) Bi 4f., (b) I 3d(c) C 1s and (d) O 1s from synthesized BiI_3 powder.

could be from glass substrate whereas the peak at 531.86 eV could be due to the C-O, C-O-O or O-H on the surface. The peak at 530.28 eV could be from the Bi-O in bismuth oxyiodide[47,48]. Thus, the XRD and XPS results together conclude to BiI_3 phase in the laboratory synthesized powder with a very little oxide impurities.

Ultrasonic spray deposited BiI_3 thin film

Structure (XRD)

X-ray diffraction of the thin film is presented in fig. 8 with appropriate indexing. The reflections in the pattern are well in match with the JCPDS card 48-1795 indicating R-3 rhombohedral BiI_3 in the trigonal crystal system. Unlike the bulk BiI_3, preferential orientation is in the (003) direction for the polycrystalline thin film. The other major intense peaks observed correspond to (006), (113),
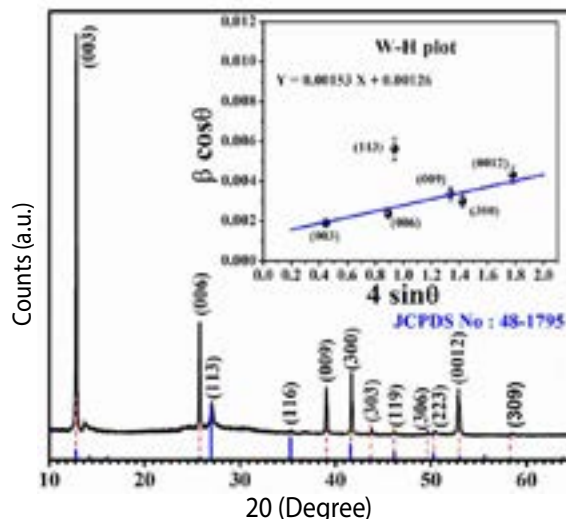

Fig. 8. XRD pattern of the spray-cast BiI_3 thin film compared with the JCPDS file of rhombohedral structure. (inset) Linear plot for Williamson-Hall equation.

103

Table 2. The structural properties derived from the X-ray diffraction analysis.

Diffracted planes	2θ (°)	FWHM (°)	Texture coefficient (TC$_{hkl}$)	Crystallite size (nm)	Average crystallite size (nm)	Crystallite size (W-H plot) (nm)	Lattice strain
(003)	12.87	0.1094	0.34	73.06			
(006)	25.78	0.1393	0.33	58.51			
(113)	27.07	0.3315	0.01	24.64	46	110	1.53 × 10^{-3}
(009)	39.05	0.2037	0.18	41.38			
(300)	41.70	0.1831	0.03	46.42			
(0012)	52.88	0.2761	0.12	32.14			

(009), (300) and (0012) planes [19,21] along with mild peaks from (116), (303), (119), (306), (223) and (309) planes. Although we have observed BiOI impurity peaks in the as-synthesized BiI$_3$ precursor powder (Fig. 5), the thin film XRD reveals phase-pure BiI$_3$. The deposition at relatively high temperature (150°C) and the rapid nucleation followed by recrystallization of BiI$_3$ has effectively suppressed the BiOI phase present in the BiI$_3$ precursor powder.

The average crystallite size (D) was calculated using the Scherrer equation (1)[49],

$$D = \frac{K\lambda}{\beta Cos\theta} \quad (1)$$

Where K is the crystallite-shape factor (~0.9 for spherical), λ is the wavelength of Cu K$_\alpha$ radiation (1.5406 Å), β is the full width at half maximum of diffraction peaks in radians and θ is the Bragg angle. Further, the Williamson-Hall (W-H) plot following the equation (2) was used for accurate crystallite size and stress calculation[50],

$$\beta Cos\theta = 4\epsilon\ sin\theta + \frac{K\lambda}{L} \quad (2)$$

Here, the broad (113) peak leads to the small R-square (0.522) of the linear fit in the W-H plot (Fig. 8 inset) from which the crystallite size was calculated to be 110 nm as compared to the 46 nm obtained from Scherrer equation. This appreciable variation in average crystallite size values suggest the presence of intrinsic strain in the structure. Such large crystallite sizes calculated from W-H plot may be comparable to the large particles observed in the SEM images. The texture coefficient represents the preferential orientation of crystallite growth in the sample which can be deduced from the equation (3),

$$TC_{hkl} = \frac{I\ (hkl)\ /I_o(hkl)}{\Sigma^N_{n=o}\ I_i(hkl)\ /I_o\ (hkl)} \quad (3)$$

where, I(hkl) is the intensity of the peak, I$_0$(hkl) is the intensity of the corresponding peak in the JCPDS file and N is the number of peaks. Table 2 displays the structural properties of the spray-coated BiI$_3$ thin film.

Morphology (SEM)

Fig. 9 displays the scanning electron micrographs of the spray deposited BiI$_3$ thin film at various magnifications. The images reveal a dendrite-like branched network spread throughout the surface. Besides, the distribution of large particles can be seen between these branches. To the best of our knowledge, such kind of interesting morphologies has never been observed in BiI$_3$ thin films. We believe that the in-situ crystallization at 150°C during the deposition might have resulted in the agglomeration of crystallites and thus the resulted morphology.

Chemical state (XPS)

The survey scan spectra of BiI$_3$ thin film with Al K$_\alpha$ radiation at room temperature in the full energy scale can be seen in fig. 10, displaying the
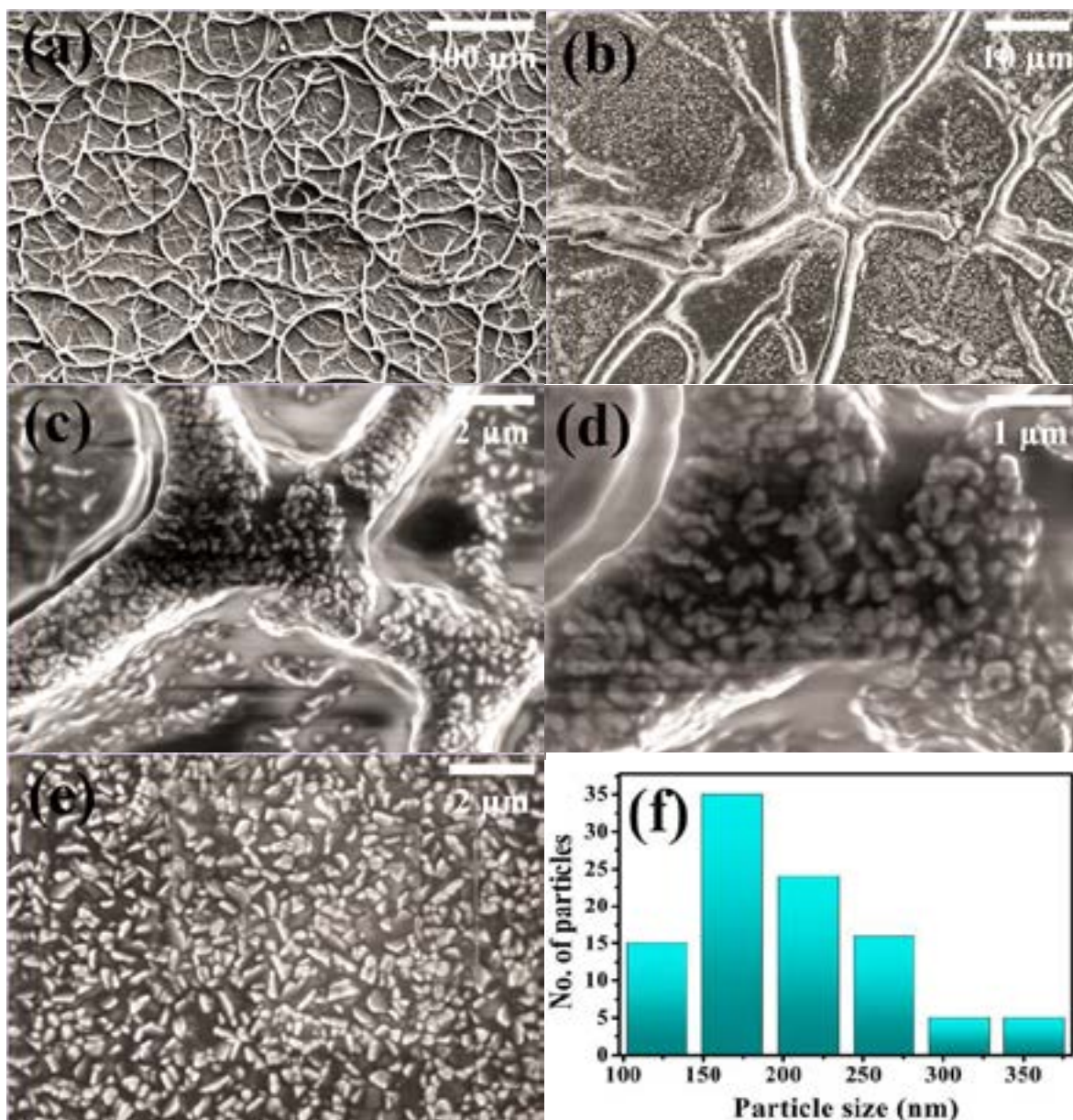
Fig. 9. (a-e) SEM images of spray-cast bismuth iodide thin film at different magnifications. (f) Particle size distribution for 100 particles measured.

important photoemission lines corresponding to Bi, I, C and O in the samples.

In order to check the relevent lines of Bi 4f, I 3d, C 1s and O 1s, high resolution scans were performed in the specified energy ranges and the obtained spectra are deconvoluted while taking care of the intensity ratios, FWHM and spin-orbit splitting.

The high-resolution Bi 4f scans show three doublets corresponding to $4f_{7/2}$ and $4f_{5/2}$ with a spin-orbit splitting of 5.3 eV (Fig. 11(a)). The peaks at 164 eV and 158.66 eV indicate the 3+ state of Bi species in BiI_3, whereas the peaks at 162.3 eV and 157 eV are due to the elemental Bi induced during the Ar-ion etching in the XPS measurement[47,51]. Besides, it is reported that long exposure to X-ray radiation can lead to more Bi^0 species in the sample[52]. Further, the peaks at 157.97 eV and 163.29 eV may have resulted from bismuth oxides formed from the long ambient exposure. However, the presence of oxides couldn't be observed in the
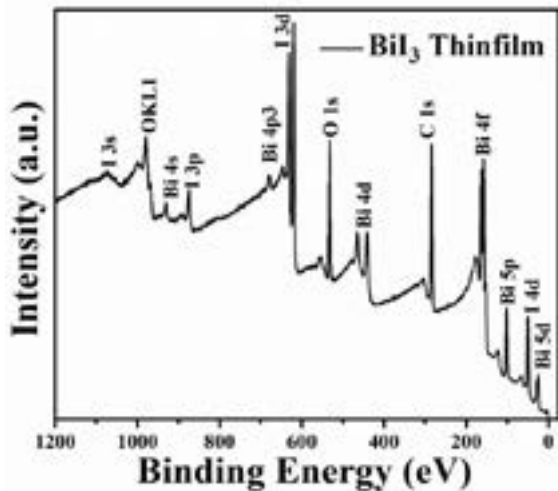
Fig. 10. The XPS survey spectrum of BiI$_3$ thin film by ultrasonic spray deposition.

XRD pattern. The peaks corresponding to I 3d$_{5/2}$ and 3d$_{3/2}$ were observed with a spin-orbit separation of 11.49 eV (Fig. 11 (b)). The peaks at 618.92 eV and 630.39 eV can be attributed to I$^-$ in BiI$_3$ thin film[51]. The peaks at 631.79 eV and 620.39 eV can be attributed to I in I$_2$[47].

Optical property (UV-Vis-NIR Spectroscopy)

The UV-Vis-NIR absorbance spectrum of BiI$_3$ thin film with an absorption edge of ~822 nm is shown in fig. 12. The absorption spectrum reveals the strong absorbing nature of the ultrasonically spray deposited BiI$_3$ thin film.

We then calculated the optical bandgap from the tauc relation (4) given by,
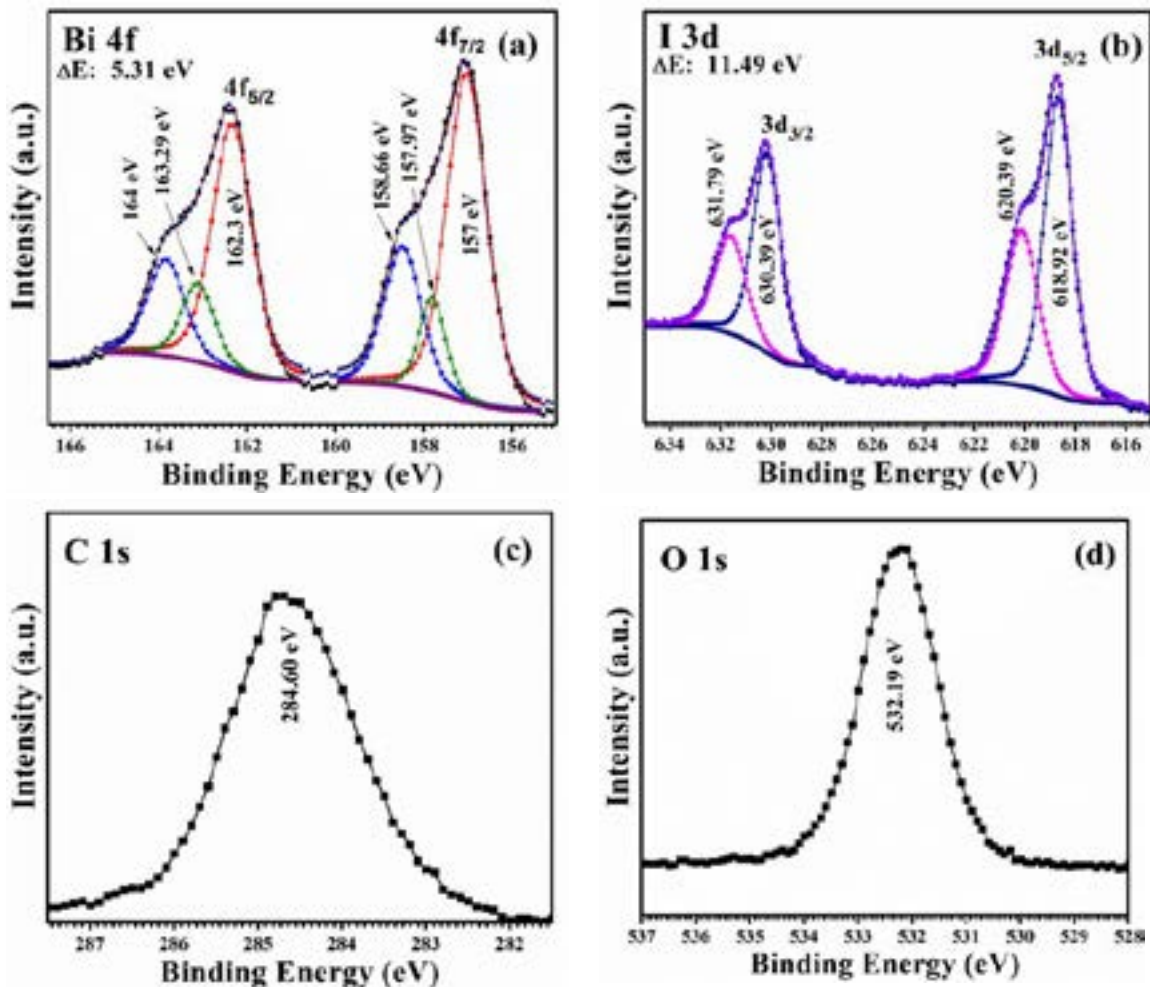

Fig. 11. High-resolution spectra of Bi 4f, I 3d, C1s and O1s states in BiI3 thin film after etching.
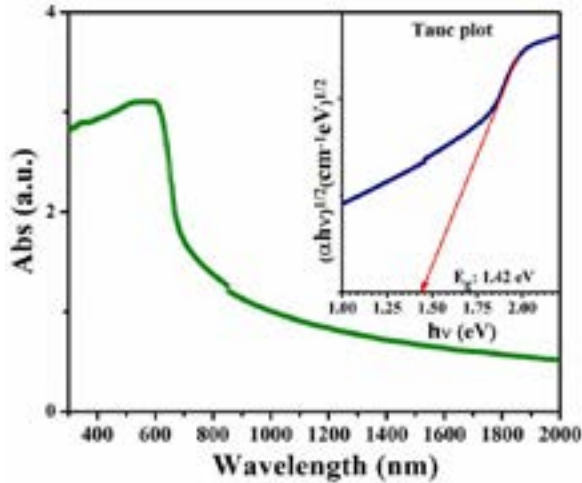
Fig. 12. The absorption spectrum of BiI$_3$ thin film. (Inset) Tauc plot showing the calculated indirect bandgap.

Where E$_g$ is the optical band gap, h is the

$$B(h\vartheta - E_g)^n = \alpha h\vartheta \qquad (4)$$

planks constant, ν is the photon frequency, B is called the band tailing parameter and n can have values corresponding to direct allowed (n=1/2), indirect allowed (n=2), direct forbidden (n=1/3) and indirect forbidden (n=3) transitions. α is the absorption coefficient which was estimated from the formula (5),

$$\alpha = \frac{1}{t} \times 2.303A \qquad (5)$$

Where, A is the absorbance and t is the thickness of the thin film which was measured to be around ~1 μm using a stylus profilometer.

The tauc plot between (αhv)$^{1/2}$ and hv reveals an indirect allowed transition of 1.42 eV which is interestingly in correlation with the 1.44 eV predicted by the DFT calculations. As discussed earlier, the lower indirect bandgap is a direct consequence of spin-orbit magnetic effects from heavy Bi and I elements in BiI$_3$. As a matter of fact, this bandgap is very close to the optimum bandgap (1.40 eV) for maximum power conversion efficiency as per the Shockley-Queisser limit[53].
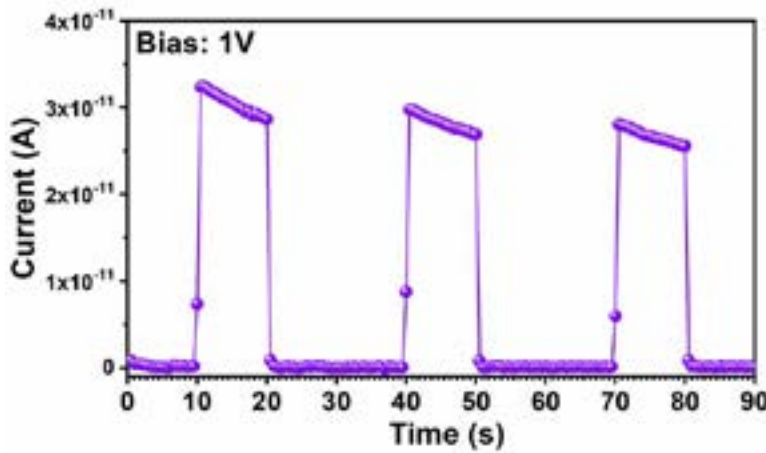

Fig. 13. Photoresponse measurement of BiI$_3$ thin film under 50 W halogen lamp.

Photoresponse

The fabricated thin films are photoconductive with a very fast response to light. The measurements were carried out under a 50 W halogen bulb and different LEDs with 1 V bias. The measurements show a dark current of 6.1×10^{-13} A which was rapidly increased to 3.1×10^{-11} A under illuminated halogen lamp (Fig. 13).
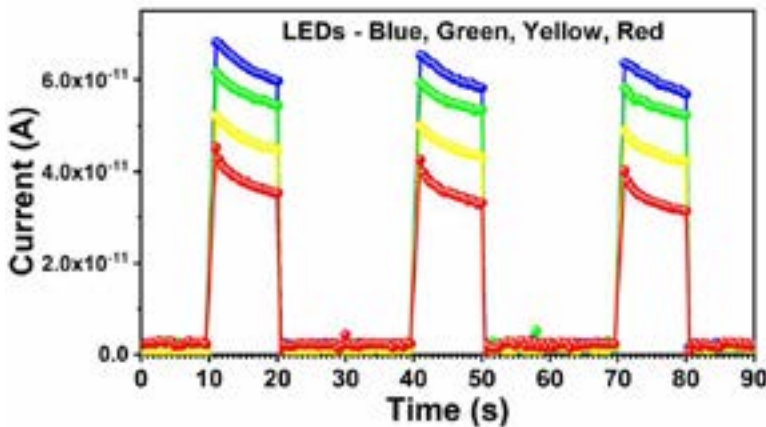
Further, we have measured the response of the film to blue, green, yellow and red LEDs (50 W) and

Fig. 14. Photoresponse measurements of BiI$_3$ film under LEDs at 1V bias. The color of the curves represent the LED wavelength.

Table 3. The sensitivity of BiI_3 thin film to different illuminations under a bias of 1 V.

Sample Illumination	I_d (pA)	I_{ph}(pA)	Sensitivity (%)
Halogen lamp	0.61	29.9	4890
Blue LED	2.24	61.1	2730
Green LED	2.24	55.0	2460
Yellow LED	2.24	45.3	2020
Red LED	2.24	36.0	1610

the results are depicted in fig. 14. The sensitivity (S) of the film under different illuminations are calculated from the equation (6)[54].

$$S\ (\%) = \frac{I_{ph}}{I_{dark}} \times 100 \qquad (6)$$

Where the photocurrent, $I_{ph} = I_{light} - I_{dark}$ The obtained data is presented in table 3.

Conclusions

DFT calculations on the BiI_3 resulted in the better understanding of the electronic structure of the material. Motivated from the computational results, BiI_3 powder was prepared and was used as a precursor for depositing thin films by the ultrasonic spray technique. The obtained phase pure films had a dendritic like morphology with an indirect band gap of 1.42 eV which was well in agreement with the DFT results. Further, the film demonstrated excellent response to illumination from halogen lamp and LEDs at low bias voltages. The interesting properties showcased by the spray deposited film are truly inspiring for further optimization and incorporation into optoelectronic devices.

Acknowledgments

References

1. Mitzi D. B., Brock P., 2001. Structure and Optical Properties of Several Organic−Inorganic Hybrids Containing Corner-Sharing Chains of Bismuth Iodide Octahedra. *Inorg. Chem. 40* (9), 2096–2104.

2. Ma F., Zhou M., Jiao Y., Gao G., Gu Y., Bilic A., Chen Z., Du A., 2015. Single Layer Bismuth Iodide: Computational Exploration of Structural, Electrical, Mechanical and Optical Properties. *Sci. Rep. 5* (1), 17558.

3. Singh D. J., 2010. Structure and Optical Properties of High Light Output Halide Scintillators. *Phys. Rev. B - Condens. Matter Mater. Phys. 82* (15).

4. Devidas T. R., Chandra Shekar N. V., Sundar C. S., Chithaiah P., Sorb Y. A., Bhadram V. S., Chandrabhas N., Pal K., Waghmare U. V., Rao C. N. R., 2014. Pressure-Induced Structural Changes and Insulator-Metal Transition in Layered Bismuth Triiodide, BiI 3 : A Combined Experimental and Theoretical Study. *J. Phys. Condens. Matter 26* (27), 275502.

5. Brandt R. E., Kurchin R. C., Hoye R. L. Z., Poindexter J. R., Wilson M. W. B., Sulekar S., Lenahan F., Yen P. X. T., Stevanović V., Nino J. C., Bawendi M. G., Buonassisi T., 2015. Investigation of Bismuth Triiodide (BiI3) for Photovoltaic Applications. *J. Phys. Chem. Lett. 6* (21), 4297–4302.

6. Kour R., Arya S., Verma S., Gupta J., Bandhoria P., Bharti V., Datt R., Gupta V., 2019. Potential Substitutes for Replacement of Lead in Perovskite Solar Cells: A Review. *Glob. Challenges 3* (11), 1900050.

7. Johansson M. B., Philippe B., Banerjee A., Phuyal D., Mukherjee S., Chakraborty S., Cameau M., Zhu H., Ahuja R., Boschloo G., Rensmo H., Johansson E. M. J., 2019. Cesium Bismuth Iodide Solar Cells from Systematic Molar Ratio Variation of CsI and BiI3. *Inorg.*

Chem. 58 (18), 12040–12052.

8. Podraza N. J., Qiu W., Hinojosa B. B., Xu H., Motyka M. A., Phillpot S. R., Baciak J. E., Trolier-McKinstry S., Nino J. C., Xu H., Motyka M. A., Phillpot S. R., Baciak J. E., Trolier-McKinstry S., Nino J. C., 2013. Band Gap and Structure of Single Crystal BiI 3 : Resolving Discrepancies in Literature. *J. Appl. Phys. 114* (3), 033110.

9. Yin W.-J., Yang J.-H., Kang J., Yan Y., Wei S.-H., 2015. Halide Perovskite Materials for Solar Cells: A Theoretical Review. *J. Mater. Chem. A 3* (17), 8926–8942.

10. Schlüter M., Cohen M. L., Kohn S. E., Fong C. Y., 1976. Electronic Structure of BiI3. *Phys. status solidi 78* (2), 737–747.

11. Yorikawa H., Muramatsu S., 2008. Theoretical Study of Crystal and Electronic Structures of BiI3. *J. Phys. Condens. Matter 20* (32).

12. Graetzel M., Janssen R. A. J., Mitzi D. B., Sargent E. H., Materials Interface Engineering for Solution-Processed Photovoltaics. *Nature*. August 16, 2012, pp 304–312.

13. Nason D., Keller L., 1995. The Growth and Crystallography of Bismuth Tri-Iodide Crystals Grown by Vapor Transport. *J. Cryst. Growth 156* (3), 221–226.

14. Jellison G. E., Ramey J. O., Boatner L. A., 1999. Optical Functions of (Formula Presented) as Measured by Generalized Ellipsometry. *Phys. Rev. B - Condens. Matter Mater. Phys. 59* (15), 9718–9721.

15. Patil T. K., Talele M. I., 2012. Comparative Study of Semiconductors Bismuth Iodate, Bismuth Triiodide and Bismuth Trisulphide Crystals. *J. Nano- Electron. Phys. 4* (4), 04003.

16. Takeyama S., Watanabe K., Komatsu T., 1990. Thin-Film Single-Crystal Growth of Bii3 by a Hot Wall Technique. *Jpn. J. Appl. Phys. 29* (4 R), 710–717.

17. Takeyama S., Watanabe K., Komatsu T., 1990. Thin-Film Single-Crystal Growth of BiI 3 by a Hot Wall Technique. *Jpn. J. Appl. Phys. 29* (Part 1, No. 4), 710–717.

18. Takeyama S., Watanabe K., Ichihara M., Suzuki K., Miura N., 1990. Van Der Waals Epitaxial Growth of Thin BiI3 Films on PbI 2 and CdI2 Substrates by a Hot Wall Method. *J. Appl. Phys. 68* (6), 2735–2738.

19. Chaudhuri T. K., Patra A. B., Basu P. K., Saraswat R. S., Acharya H. N., 1989. Preparation of Bismuth Iodide Thin Films by a Chemical Method. *Mater. Lett. 8* (9), 361–363.

20. Coutinho N. F., Merlo R. B., Borrero N. F. V., Marques F. C., 2018. Thermal Evaporated Bismuth Triiodide (BiI3) Thin Films for Photovoltaic Applications. *MRS Adv. 3* (55), 3233–3236.

21. Coutinho N. F., Cucatti S., Merlo R. B., Silva Filho J. M. C., Villegas N. F. B., Alvarez F., Nogueira A. F., Marques F. C., 2019. The Thermomechanical Properties of Thermally Evaporated Bismuth Triiodide Thin Films. *Sci. Rep. 9* (1), 11785.

22. Cuña A., Aguiar I., Gancharov A., Pérez M., Fornaro L., 2004. Correlation between Growth Orientation and Growth Temperature for Bismuth Tri-Iodide Films. *Cryst. Res. Technol. 39* (10), 899–905.

23. Kodzasa T., Ushijima H., Matsuda H., Kamata T., 2000. Preparation of Thin Film of Layer Structured Bismuth Iodide with a Long Chain Alkylammonium and Its Nonlinear Optical Property. *Mol. Cryst. Liq. Cryst. Sci. Technol. Sect. A. Mol. Cryst. Liq. Cryst. 343* (1), 71–75.

24. Hamdeh U. H., Nelson R. D., Ryan B. J., Bhattacharjee U., Petrich J. W., Panthani M. G., 2016. Solution-Processed BiI3 Thin Films for Photovoltaic Applications: Improved Carrier Collection via Solvent Annealing. *Chem. Mater. 28* (18), 6567–6574.

25. Bishop J. E., Read C. D., Smith J. A., Routledge T. J., Lidzey D. G., 2020. Fully Spray-Coated Triple-Cation Perovskite Solar Cells. *Sci. Rep. 10* (1), 6610.

26. Bishop J. E., Mohamad D. K., Wong-Stringer M., Smith A., Lidzey D. G., 2017. Spray-Cast Multilayer Perovskite Solar Cells with an Active-Area of 1.5 Cm2. *Sci. Rep. 7* (1), 1–11.

27. Mohamad D. K., Griffin J., Bracher C., Barrows

A. T., Lidzey D. G., 2016. Spray-Cast Multilayer Organometal Perovskite Solar Cells Fabricated in Air. *Adv. Energy Mater. 6* (22), 1600994.

28. Barrows A. T., Pearson A. J., Kwak C. K., Dunbar A. D. F., Buckley A. R., Lidzey D. G., 2014. Efficient Planar Heterojunction Mixed-Halide Perovskite Solar Cells Deposited via Spray-Deposition. *Energy Environ. Sci. 7* (9), 2944–2950.

29. Huang H., Shi J., Zhu L., Li D., Luo Y., Meng Q., 2016. Two-Step Ultrasonic Spray Deposition of CH3NH3PbI3 for Efficient and Large-Area Perovskite Solar Cell. *Nano Energy 27*, 352–358.

30. Heo J. H., Lee M. H., Jang M. H., Im S. H., 2016. Highly Efficient CH3NH3PbI3−xClx Mixed Halide Perovskite Solar Cells Prepared by Re-Dissolution and Crystal Grain Growth via Spray Coating. *J. Mater. Chem. A 4* (45), 17636–17642.

31. Chou L. H., Wang X. F., Osaka I., Wu C. G., Liu C. L., 2018. Scalable Ultrasonic Spray-Processing Technique for Manufacturing Large-Area CH 3 NH 3 PbI 3 Perovskite Solar Cells. *ACS Appl. Mater. Interfaces 10* (44), 38042–38050.

32. Ulična S., Dou B., Kim D. H., Zhu K., Walls J. M., Bowers J. W., Van Hest M. F. A. M., 2018. Scalable Deposition of High-Efficiency Perovskite Solar Cells by Spray-Coating. *ACS Appl. Energy Mater. 1* (5), 1853–1857.

33. Bishop J. E., Smith J. A., Greenland C., Kumar V., Vaenas N., Game O. S., Routledge T. J., Wong-Stringer M., Rodenburg C., Lidzey D. G., 2018. High-Efficiency Spray-Coated Perovskite Solar Cells Utilizing Vacuum-Assisted Solution Processing. *ACS Appl. Mater. Interfaces 10* (46), 39428–39434.

34. Su J., Cai H., Ye X., Zhou X., Yang J., Wang D., Ni J., Li J., Zhang J., 2019. Efficient Perovskite Solar Cells Prepared by Hot Air Blowing to Ultrasonic Spraying in Ambient Air. *ACS Appl. Mater. Interfaces 11* (11), 10689–10696.

35. Park M., Cho W., Lee G., Hong S. C., Kim M. cheol, Yoon J., Ahn N., Choi M., 2019. Highly Reproducible Large-Area Perovskite Solar Cell Fabrication via Continuous Megasonic Spray Coating of CH3NH3PbI3. *Small 15* (1), 1804005.

36. Perdew J. P., Burke K., Ernzerhof M., 1996. Generalized Gradient Approximation Made Simple. *Phys. Rev. Lett. 77* (18), 3865–3868.

37. Kresse G., Furthmüller J., 1996. Efficiency of Ab-Initio Total Energy Calculations for Metals and Semiconductors Using a Plane-Wave Basis Set. *Comput. Mater. Sci. 6* (1), 15–50.

38. Kresse G., Furthmüller J., 1996. Efficient Iterative Schemes for Ab Initio Total-Energy Calculations Using a Plane-Wave Basis Set. *Phys. Rev. B - Condens. Matter Mater. Phys. 54* (16), 11169–11186.

39. MedeA® 3.0 Software, Materials Design Inc., San Diego, CA, USA. Materials Design Inc.: San Diego, CA, USA 2018.

40. Joubert D., 1999. From Ultrasoft Pseudopotentials to the Projector Augmented-Wave Method. *Phys. Rev. B - Condens. Matter Mater. Phys. 59* (3), 1758–1775.

41. Ultrasonic Spray Pyrolysis https://www.cysi.wang/Electrospinning/Ultrasonic-atomization-pyrolysis-spraying-system.html (accessed Mar 15, 2020).

42. Lehner A. J., Wang H., Fabini D. H., Liman C. D., Hébert C.-A., Perry E. E., Wang M., Bazan G. C., Chabinyc M. L., Seshadri R., 2015. Electronic Structure and Photovoltaic Application of BiI 3. *Appl. Phys. Lett. 107* (13), 131109.

43. Hoang K., Mahanti S. D., Salvador J. R., Kanatzidis M. G., 2007. Atomic Ordering and Gap Formation in Ag-Sb-Based Ternary Chalcogenides. *Phys. Rev. Lett. 99* (15), 1–4.

44. Lehner A. J., Wang H., Fabini D. H., Liman C. D., Hébert C. A., Perry E. E., Wang M., Bazan G. C., Chabinyc M. L., Seshadri R., 2015. Electronic Structure and Photovoltaic Application of BiI3. *Appl. Phys. Lett. 107* (13), 131109.

45. Brandt R. E., Kurchin R. C., Hoye R. L. Z., Poindexter J. R., Wilson M. W. B., Sulekar S., Lenahan F., Yen P. X. T., Stevanović V., Nino J. C., Bawendi M. G., Buonassisi T., 2015. Investigation of Bismuth Triiodide (BiI 3) for

Photovoltaic Applications. *J. Phys. Chem. Lett. 6* (21), 4297–4302.

46. Johansson M. B., Zhu H., Johansson E. M. J., 2016. Extended Photo-Conversion Spectrum in Low-Toxic Bismuth Halide Perovskite Solar Cells. *J. Phys. Chem. Lett. 7* (17), 3467–3471.

47. Moulder J. F., Stickle W. F., Sobol P. E., Bomben K. D., *Handbook of X-Ray Photoelectron Spectroscopy: A Reference Book of Standard Spectra for Identification and Interpretation of XPS Data*.

48. Wang Y., Deng K., Zhang L., 2011. Visible Light Photocatalysis of BiOI and Its Photocatalytic Activity Enhancement by in Situ Ionic Liquid Modification. *J. Phys. Chem. C 115* (29), 14300–14308.

49. SCHERRER, P., 1918. Nachr Ges Wiss Goettingen. *Math. Phys. 2*, 98–100.

50. Monshi A., Foroughi M. R., Monshi M. R., 2012. Modified Scherrer Equation to Estimate More Accurately Nano-Crystallite Size Using XRD. *World J. Nano Sci. Eng. 02* (03), 154–160.

51. Boopathi K. M., Raman S., Mohanraman R., Chou F.-C., Chen Y.-Y., Lee C.-H., Chang F.-C., Chu C.-W., Moorthy Boopathi K., Raman S., Mohanraman R., Chou F.-C., Chen Y.-Y., Lee C.-H., Chang F.-C., Chu C.-W., 2014. Solution-Processable Bismuth Iodide Nanosheets as Hole Transport Layers for Organic Solar Cells. *Sol. Energy Mater. Sol. Cells 121*, 35–41.

52. Fabian D. M., Ardo S., 2016. Hybrid Organic–Inorganic Solar Cells Based on Bismuth Iodide and 1,6-Hexanediammonium Dication. *J. Mater. Chem. A 4* (18), 6837–6841.

53. Shockley W., Read W. T., 1952. Statistics of the Recombination of Holes and Electrons. *Phys. Rev. 87* (46), 835–842.

54. Hemanth Kumar B., Shaji S., Santhosh Kumar M. C., 2019. Fabrication of Visible Light Photodetector Using Co-Evaporated Indium Sulfide Thin Films. *J. Mater. Sci. Mater. Electron. 30* (19), 17986–17998.

Scientia (Annual)